

Spatio-angular fluorescence microscopy I. Basic theory

TALON CHANDLER,^{1,*} AUTHOR ORDER TBD,^{2,*} AND PATRICK LA
RIVIÈRE¹

¹University of Chicago, Department of Radiology, Chicago, Illinois 60637, USA

²Publications Department, The Optical Society, 2010 Massachusetts Avenue NW, Washington, DC 20036, USA

³Currently with the Department of Electronic Journals, The Optical Society, 2010 Massachusetts Avenue NW, Washington, DC 20036, USA

*talonchandler@talonchandler.com

Abstract: We introduce the basic elements of a spatio-angular theory of fluorescence microscopy. We start by modeling a microscope imaging an ensemble of in-focus fluorescent dipoles as a linear Hilbert-space operator with domain $L_2(\mathbb{R}^2 \times \mathbb{S}^2)$ and range $L_2(\mathbb{R}^2)$, and we express the operator in terms of four different sets of object-space basis functions. We show that the operator takes a particularly convenient form when expressed in a basis of spatial and spherical harmonics—a form we call the spatio-angular transfer function (SATF). We demonstrate our formalism by analyzing a paraxial single-view fluorescence microscope without using the monopole or scalar approximations. We show that this microscope has an angular band limit, and we demonstrate the value of the transfer function approach by efficiently simulating the imaging process with numerical phantoms. Notably, we show that information about the out-of-plane orientation of ensembles of in-focus fluorophores is imaged in paraxial widefield fluorescence microscopes. We discuss the implications of our analysis for all quantitative fluorescence microscopy studies and lay out a path towards a complete theory.

1. Introduction **needs work**

Fluorescence microscopes are widely used in the biological sciences for measuring the distribution of fluorophores throughout a sample [cite]. While an unprocessed fluorescence micrograph reports the approximate distribution of fluorophores throughout a sample, all microscopes are diffraction limited [cite], so the image is a blurred version of the true fluorophore distribution. Therefore, microscopists who are interested in optimal measurements will perform a computational restoration to recover some of the information lost during the imaging process.

Restoration techniques attempt to recover the true distribution of fluorophores using the measured data and a model of the imaging process. A model of the imaging process can be obtained theoretically (by mathematically modeling the instrument under idealized conditions), experimentally (by measuring the instrument’s response to a known input), or by a combination of theory and experiment (by measuring parameters of an instrument model). In all cases the accuracy of the restored fluorophore distribution is limited by the accuracy of the imaging model. All theoretical imaging models make simplifying approximations that limit the accuracy of restorations, so it is important to verify that the approximations introduce an acceptable level of error. This work investigates the errors introduced by two common approximations in models of fluorescence microscopes—the *monopole approximation* and the *scalar approximation*.

This work lies at the intersection of three classes of fluorescence microscopy: (1) single-molecule localization microscopy (SMLM), (2) spatial ensemble fluorescence microscopy including widefield, confocal, and light-sheet techniques, and (3) polarized fluorescence microscopy. We briefly review these three classes and focus on their restoration techniques and use of the monopole and scalar approximations.

The SMLM community has pioneered the use of rigorous electromagnetic models of fluores-

cence microscopes [1, 2] [cite Novotny]. When a single molecule is fluorescing in the sample, the measured intensity pattern is strongly dependent on the orientation of the emitting molecule. Backlund and Lew [3] have shown that ignoring the orientation of fluorophores can bias position estimates, so the most accurate SMLM experiments must jointly estimate the position and orientation of each molecule.

Meanwhile, most fluorescence microscopists image ensembles of fluorophores and restore their images without considering the role that the monopole and scalar approximations play in the restoration process. A typical fluorescence microscopist is only interested in the spatial distribution of fluorophores, so they reason that they can ignore the orientation of the emitters.

A smaller community of microscopists is interested in measuring the orientation of ensembles of fluorophores [4] [Forkey, Goldman, Moerner, Oldenbourg]. These techniques typically use polarized illumination or polarized detection to make multiple measurements of the same object. Current angular restoration techniques use a model of the dipole excitation and emission processes [Fourkas] to recover the orientation of fluorophores using pixel-wise arithmetic, but these techniques do not perform any spatial restoration so they do not use all of the information available to the microscopist. To our knowledge no work has been done to model the complete spatio-angular response of fluorescence microscopes to ensembles of oriented fluorophores.

Out of date In this work we model ensembles of in-focus dipole absorber/emitters using electromagnetic optics and the paraxial approximation. In section 2 we model the excitation and detection processes of dipoles, and we define the most important quantity in this work—the spatio-angular transfer function (SATF). We calculate the SATF and show that fluorescence microscopes have an angular band limit. In section 3 we perform simulations and compare our model to traditional scalar models. In section 4 we discuss the implications of our work for fluorescence microscopy and lay out a path towards a complete spatio-angular theory of fluorescence microscopy.

1.1. Monopole emission vs. dipole emission *not sure where this section should live*

Consider a single dipole radiator at the origin with its dipole moment oriented along a direction $\hat{\mathbf{s}}_o$. The dipole emitter creates a time-harmonic electric field at a position \mathbf{r} far from the dipole proportional to

$$\mathbf{E}_{\text{ff}}(\mathbf{r}, \hat{\mathbf{s}}_o) \propto \frac{\exp[ik|\mathbf{r}|]}{|\mathbf{r}|} \hat{\mathbf{r}} \times \hat{\mathbf{s}}_o \times \hat{\mathbf{r}}. \quad (1)$$

A typical approach to deriving Equation 1 is to (1) use Maxwell’s equations to derive the inhomogeneous electromagnetic wave equations then (2) use potentials to solve the wave equations with a dipole source term, then (3) drop the terms that decay faster than $1/|\mathbf{r}|$ [cite Jackson, Novotny, Teich]. Equation 1 shows that dipole radiators emit spherical wavefronts of polarized light with amplitude proportional to $\cos \theta$ where θ is the angle between the field point \mathbf{r} and the dipole axis $\hat{\mathbf{s}}_o$.

Many models of fluorophores approximate the vector field on the left hand side of Equation 1 with a scalar field—the *scalar approximation*—and drop the orientation dependence on the right hand side—the *monopole approximation*. The approximated field is given by

$$U_{\text{ff}}(\mathbf{r}) \propto \frac{\exp[ik|\mathbf{r}|]}{|\mathbf{r}|}. \quad (2)$$

Models that use Equation 2 as a starting point do not account for polarization or dipole orientation effects.

2. Theory outline is okay, subsections vary, recently moved changes of basis to the front

We begin our analysis with the abstract Hilbert space formalism of Barrett and Myers [5]. Our first task is to formulate the imaging process as a mapping between two Hilbert spaces $\mathcal{H} : \mathbb{U} \rightarrow \mathbb{V}$ where \mathbb{U} is a set that contains all possible objects, \mathbb{V} is a set that contains all possible datasets, and \mathcal{H} is a model of the instrument that maps between these two spaces. We denote (possibly infinite-dimensional) Hilbert-space vectors in \mathbb{U} with \mathbf{f} , Hilbert-space vectors in \mathbb{V} with \mathbf{g} , and the mapping between the spaces with

$$\mathbf{g} = \mathcal{H}\mathbf{f}. \quad (3)$$

Once we have identified the spaces \mathbb{U} and \mathbb{V} , we can start expressing the mapping between the spaces in a specific object-space and data-space basis. In most cases the easiest mapping to find uses a delta-function basis—we expand object and data space into delta functions then express the mapping as an integral transform. After finding this mapping we can start to investigate the same mapping in different bases.

The above discussion is quite abstract, but it is a powerful point of view that will enable us to draw new conclusions about all fluorescence microscopes. In Section 2.1 we will demonstrate the formalism by examining a familiar monopole imaging model, and we will show that the point spread function and the optical transfer function are mappings between object and data space expressed in two different bases. In Section 2.2 we will extend the monopole imaging model to dipoles and examine the mapping in four different bases. In Section 2.3 we will examine the mappings for a more specific case—a paraxial epi-illumination single-view fluorescence microscope.

2.1. Monopole imaging in different bases 50%

We start by considering a microscope that images a field of in-focus monopoles by recording the irradiance on a two-dimensional detector. We can represent the object as a function that assigns a real number to each point on a plane, so we identify object space as $\mathbb{U} = \mathbb{L}_2(\mathbb{R}^2)$. Similarly, we have a two-dimensional detector that measures a real number at every point on a plane, so data space is the same set $\mathbb{V} = \mathbb{L}_2(\mathbb{R}^2)$. Our first task is complete—we have identified the geometry of object and data space.

Next, we find and name the representations of our object and data in a specific basis. In a delta function basis the object can be represented by a function $f(\mathbf{r}_o)$ called the *monopole density*—the number of monopoles at the two-dimensional position \mathbf{r}_o per unit area. Similarly, in a delta function basis the data can be represented by a function $g(\mathbf{r}_d)$ called the *irradiance*—the power received by a surface at position \mathbf{r}_d per unit area. It may seem pedantic to emphasize that these representations are in a delta function basis, but we highlight this point to make it clear that the delta function basis is not special—we can choose a different basis at will.

A reasonable starting point is to assume that the relationship between the object and the data is *linear*—this is usually true in fluorescence microscopes since fluorophores emit incoherently so a scaled sum of fluorophores will result in a scaled sum of the irradiance patterns created by the individual fluorophores. If the mapping is linear we can write the irradiance as the integral over a field of monopoles weighted by the detector response due to single monopoles

$$g(\mathbf{r}_d) = \int_{\mathbb{R}^2} d\mathbf{r}_o h(\mathbf{r}_d, \mathbf{r}_o) f(\mathbf{r}_o), \quad (4)$$

where $h(\mathbf{r}_d, \mathbf{r}_o)$ is the kernel of the integral transform.

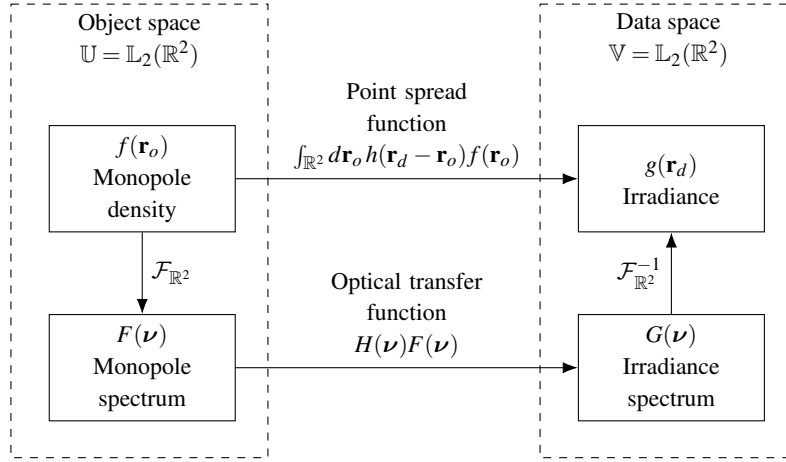


Fig. 1. We can compute the mapping between object space and data space using two different bases.

Most fluorescence microscopes are (at least approximately) shift-invariant, which means that shifting the object will result in a corresponding shift of the data. The mapping between an object and the data in a linear shift-invariant fluorescence microscope can be written as

$$g(\mathbf{r}_d) = \int_{\mathbb{R}^2} d\mathbf{r}_o h(\mathbf{r}_d - \mathbf{r}_o) f(\mathbf{r}_o). \quad (5)$$

When the imaging system is shift invariant the kernel $h(\mathbf{r}_d - \mathbf{r}_o)$ is usually called the *point spread function*.

The mapping between the object and the data in linear shift-invariant microscopes takes a particularly simple form in a spatial harmonic basis. If we apply the Fourier convolution theorem to Eq. 5 we find that

$$G(\mathbf{v}) = H(\mathbf{v}) F(\mathbf{v}), \quad (6)$$

where the *irradiance spectrum* is given by

$$G(\mathbf{v}) = \int_{\mathbb{R}^2} d\mathbf{r} g(\mathbf{r}) \exp(-2\pi i \mathbf{r} \cdot \mathbf{v}), \quad (7)$$

the *optical transfer function* is given by

$$H(\mathbf{v}) = \int_{\mathbb{R}^2} d\mathbf{r} h(\mathbf{r}) \exp(-2\pi i \mathbf{r} \cdot \mathbf{v}), \quad (8)$$

and the *monopole spectrum* is given by

$$F(\mathbf{v}) = \int_{\mathbb{R}^2} d\mathbf{r} f(\mathbf{r}) \exp(-2\pi i \mathbf{r} \cdot \mathbf{v}). \quad (9)$$

Notice that Eqs. 5 and 6 are expressions of the same mapping between object and data space in different bases. Figure 1 summarizes the relationship between object and data space in both bases.

2.2. Dipole imaging in different bases 50%

Now we consider a microscope imaging a field of in-focus *dipoles* by recording the irradiance on a two-dimensional detector. A function that assigns a real number to each point on a plane is not sufficient to specify a field of dipoles because the dipoles can have different orientations. To represent the object we need to extend object space to $\mathbb{U} = \mathbb{L}_2(\mathbb{R}^2 \times \mathbb{S}^2)$ where \mathbb{S}^2 is the two-dimensional sphere (the usual sphere embedded in \mathbb{R}^3).

In a delta function basis the object can be represented by a function $f(\mathbf{r}_o, \hat{\mathbf{s}}_o)$ called the *spatio-angular density*—the number of dipoles at position \mathbf{r}_o per unit area oriented along $\hat{\mathbf{s}}_o$ per unit solid angle. If the imaging system is linear and shift invariant then the mapping between object and data space can be expressed in a delta function basis as

$$g(\mathbf{r}_d) = \int_{\mathbb{S}^2} d\hat{\mathbf{s}}_o \int_{\mathbb{R}^2} d\mathbf{r}_o h(\mathbf{r}_d - \mathbf{r}_o, \hat{\mathbf{s}}_o) f(\mathbf{r}_o, \hat{\mathbf{s}}_o), \quad (10)$$

where $h(\mathbf{r}_d - \mathbf{r}_o, \hat{\mathbf{s}}_o)$ is the *orientation-dependent point spread function*.

We can make our first change of basis by applying the Fourier-convolution theorem to Eq. 10 which yields

$$G(\mathbf{v}) = \int_{\mathbb{S}^2} d\hat{\mathbf{s}} H(\mathbf{v}, \hat{\mathbf{s}}) F(\mathbf{v}, \hat{\mathbf{s}}), \quad (11)$$

where we define the *irradiance spectrum* as

$$G(\mathbf{v}) = \int_{\mathbb{R}^2} d\mathbf{r} g(\mathbf{r}) \exp(-2\pi i \mathbf{r} \cdot \mathbf{v}), \quad (12)$$

the *orientation-dependent optical transfer function* as

$$H(\mathbf{v}, \hat{\mathbf{s}}) = \int_{\mathbb{R}^2} d\mathbf{r} h(\mathbf{r}, \hat{\mathbf{s}}) \exp(-2\pi i \mathbf{r} \cdot \mathbf{v}), \quad (13)$$

and the *spatial density spectrum* as

$$F(\mathbf{v}, \hat{\mathbf{s}}) = \int_{\mathbb{R}^2} d\mathbf{r} f(\mathbf{r}, \hat{\mathbf{s}}) \exp(-2\pi i \mathbf{r} \cdot \mathbf{v}). \quad (14)$$

This basis is well suited for simulating objects that are angularly sparse and spatially dense.

The spherical harmonics provide another set of convenient basis functions. We can change basis from spherical delta functions to spherical harmonics by making use of the generalized Plancharel theorem for spherical functions

$$\int_{\mathbb{S}^2} d\hat{\mathbf{s}} h(\hat{\mathbf{s}}) f(\hat{\mathbf{s}}) = \sum_{\ell=0}^{\infty} \sum_{m=-\ell}^{\ell} H_{\ell}^m F_{\ell}^m, \quad (15)$$

where

$$F_{\ell}^m \equiv \int_{\mathbb{S}^2} d\hat{\mathbf{s}} f(\hat{\mathbf{s}}) \bar{Y}_{\ell}^m(\hat{\mathbf{s}}), \quad (16)$$

is the spherical Fourier transform of $f(\hat{\mathbf{s}})$, \bar{z} denotes the complex conjugate of z , and $Y_{\ell}^m(\hat{\mathbf{s}})$ are the spherical harmonic functions defined in Appendix B. Eq. 15 expresses the fact that scalar products are invariant under a change of basis (see Eq. 3.78 of [5]). The left-hand side of Eq. 15 is the scalar product of $\mathbb{L}_2(\mathbb{S}^2)$ functions in a delta function basis and the right hand side is the

scalar product of $\mathbb{L}_2(\mathbb{S}^2)$ functions in a spherical harmonic function basis. Applying Eq. 15 to Eq. 10 yields

$$g(\mathbf{r}_d) = \sum_{\ell=0}^{\infty} \sum_{m=-\ell}^{\ell} H_{\ell}^m(\mathbf{r}_d - \mathbf{r}_o) F_{\ell}^m(\mathbf{r}_o) \quad (17)$$

where we have defined the *angular transfer function* as

$$H_{\ell}^m(\mathbf{r}) = \int_{\mathbb{S}^2} d\hat{\mathbf{s}} h(\mathbf{r}, \hat{\mathbf{s}}) \bar{Y}_{\ell}^m(\hat{\mathbf{s}}), \quad (18)$$

and the *angular density spectrum* as

$$F_{\ell}^m(\mathbf{r}) = \int_{\mathbb{S}^2} d\hat{\mathbf{s}} f(\mathbf{r}, \hat{\mathbf{s}}) \bar{Y}_{\ell}^m(\hat{\mathbf{s}}). \quad (19)$$

This basis is well suited for simulating objects that are spatially sparse and angularly dense.

We can arrive at our final basis in two ways: by applying the generalized Plancharel theorem for spherical functions to Eq. 11 or by applying the Fourier convolution theorem to Eq. 17. We follow the second path and find that

$$G(\mathbf{v}) = \sum_{\ell=0}^{\infty} \sum_{m=-\ell}^{\ell} H_{\ell}^m(\mathbf{v}) F_{\ell}^m(\mathbf{v}), \quad (20)$$

where we have defined the *spatio-angular transfer function* (SATF) as

$$H_{\ell}^m(\mathbf{v}) \equiv \int_{\mathbb{S}^2} d\hat{\mathbf{s}} H(\mathbf{v}, \hat{\mathbf{s}}) \bar{Y}_{\ell}^m(\hat{\mathbf{s}}), \quad (21)$$

and the *spatio-angular density spectrum* as

$$F_{\ell}^m(\mathbf{v}) \equiv \int_{\mathbb{S}^2} d\hat{\mathbf{s}} F(\mathbf{v}, \hat{\mathbf{s}}) \bar{Y}_{\ell}^m(\hat{\mathbf{s}}). \quad (22)$$

This basis is well suited for simulating arbitrary samples because it exploits the sparsity of the imaging system—we will see this explicitly when we calculate a specific case of the spatio-angular transfer function.

Figure 2 summarizes the relationship between the four bases that we can use to compute the image of a field of dipoles.

2.3. Paraxial epi-fluorescence microscope

This section is probably the most mature, but it still has some mismatch with newer sections. I've quit using "kernel" and haven't fixed it. In this section we apply the tools we developed in the previous two sections to analyze a paraxial epi-fluorescence microscope. We start by reviewing the derivation of the monopole point spread function in preparation for the derivation of the orientation-dependent point spread function. We conclude the section by analyzing the dipole imaging map in the four bases we described earlier.

2.3.1. Monopole point spread function

In this section we derive the form of the monopole point spread function $h(\mathbf{r})$. First, we place a monopole emitter at the focal point of an objective lens and calculate the field created in the back focal plane. We can model a paraxial thin lens as a quadratic phase element, so it converts a

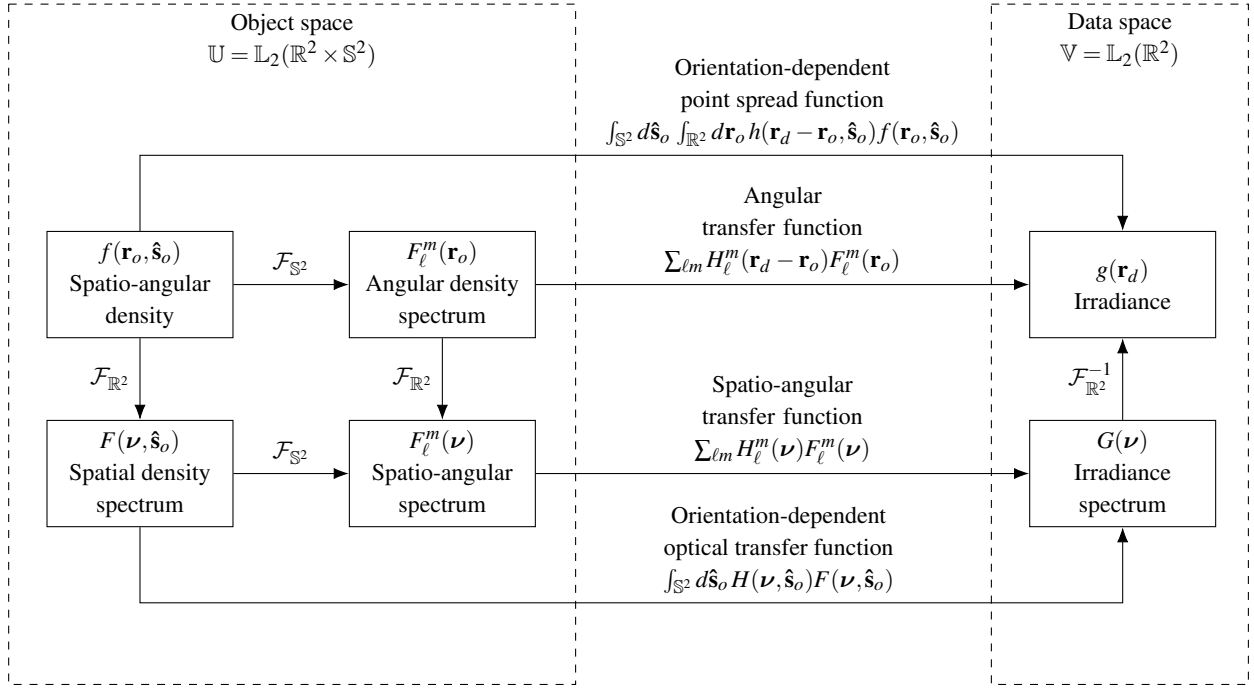


Fig. 2. We can compute the mapping between object space and data space using four different bases.

spherical wave to a plane wave in the back focal plane with a sharp cutoff at the exit pupil of the lens

$$U_{\text{bfp}}(\mathbf{r}_b) \propto \Pi\left(\frac{|\mathbf{r}_b|}{\alpha}\right) \equiv \begin{cases} 1 & \text{if } |\mathbf{r}_b| < \alpha, \\ 0 & \text{else.} \end{cases} \quad (23)$$

A central result of Fourier optics is that the fields one focal distance from either side of a paraxial lens are related by a scaled two-dimensional Fourier transform. If we place a detector in the focal plane of the tube lens then the field on the detector is given by

$$U_{\text{det}}(\mathbf{r}_d) \propto \mathcal{F}_{\mathbb{R}^2} \{U_{\text{bfp}}(\mathbf{r}_b)\} = \frac{J_1(k\alpha|\mathbf{r}_d|)}{k\alpha|\mathbf{r}_d|}. \quad (24)$$

Finally, the detector measures the irradiance instead of the field, so we take the modulus squared of the field to find that the measurable irradiance created by a single monopole radiator at the origin is the familiar Airy disk

$$h(\mathbf{r}_d, \mathbf{r}_o = 0) \propto |U_{\text{det}}(\mathbf{r}_d)|^2 = \left[\frac{J_1(k\alpha|\mathbf{r}_d|)}{k\alpha|\mathbf{r}_d|} \right]^2. \quad (25)$$

Shifting the monopole in the transverse plane will introduce a linear phase factor in the back focal plane which will manifest as a shift on the detector due to the Fourier shift theorem. Therefore, the monopole imaging system is shift invariant and we can rewrite the irradiance on the detector due to a monopole at \mathbf{r}_o as

$$h(\mathbf{r}_d, \mathbf{r}_o) = h(\mathbf{r}_d - \mathbf{r}_o). \quad (26)$$

We have modeled a microscope with unit magnification, but a similar point spread function can be found for magnifying microscopes by making a change of variables—see Barrett section 7.2.7.

Rotating a monopole will leave its image unchanged. Therefore, our imaging system is rotation invariant and we can simplify the orientation-dependent point spread function further with

$$h(\mathbf{r}_d - \mathbf{r}_o) = h(|\mathbf{r}_d - \mathbf{r}_o|). \quad (27)$$

2.3.2. Orientation-dependent point spread function

In the next two subsections we will calculate the orientation dependent point spread function $h(\mathbf{r}, \hat{\mathbf{s}})$ of a paraxial epi-fluorescence microscope. We can make our first simplifying step by realizing the excitation and detection processes are incoherent which means that the orientation-dependent PSF is separable

$$h(\mathbf{r}_d, \mathbf{r}_o, \hat{\mathbf{s}}_o) = h_{\text{exc}}(\mathbf{r}_o, \hat{\mathbf{s}}_o) h_{\text{det}}(\mathbf{r}_d, \mathbf{r}_o, \hat{\mathbf{s}}_o). \quad (28)$$

We can calculate the excitation and detection PSFs separately then take their product to find the complete orientation-dependent PSF.

2.3.3. Dipole excitation model

When we developed the monopole imaging model we ignored the excitation process because we excited the fluorophores with a spatially uniform excitation beam and monopoles have no orientation dependence. For the dipole imaging model we must model the excitation process because the excitation process is rarely angularly uniform (carefully calibrated TIRF systems are an exception).

In this section we will calculate the excitation kernel $h_{\text{exc}}(\mathbf{r}_o, \hat{\mathbf{s}}_o)$ for the paraxial epi-illumination microscope under unpolarized Köehler illumination shown in Figure 7. We will only consider spatially uniform excitation, so the excitation kernel will no depend on \mathbf{r}_o

$$h_{\text{exc}}(\mathbf{r}_o, \hat{\mathbf{s}}_o) = h_{\text{exc}}(\hat{\mathbf{s}}_o). \quad (29)$$

We can interpret $h_{\text{exc}}(\hat{\mathbf{s}}_o)$ as the relative probability of exciting a molecule with dipole orientation $\hat{\mathbf{s}}_o$. Our approach is similar to previous work [6, 7], but here we consider paraxial, incoherent, and unpolarized illumination.

We start by expressing the dipole moment $\hat{\mathbf{s}}_o$ in Cartesian coordinates

$$\hat{\mathbf{s}}_o = s_x \hat{\mathbf{x}} + s_y \hat{\mathbf{y}} + s_z \hat{\mathbf{z}}. \quad (30)$$

We place the dipole in the focal plane of an aplanatic and polarization-preserving objective lens with its optical axis aligned with the $\hat{\mathbf{z}}$ axis. Next, we place a spatially incoherent, spatially uniform, unpolarized light source (or its image) in the back aperture of the objective lens to illuminate the focal plane. In this geometry each point in the back focal plane generates a plane wave that illuminates the sample.

To model the unpolarized light source we will use polarized ray tracing [8] to find the response for a single polarized ray, then integrate over the rays and polarizations to find the complete response. First, we model the electric field at every point on the back focal plane as

$$\mathbf{E}_{\text{bfp}}(\phi_{\text{pol}}) \propto \cos \phi_{\text{pol}} \hat{\mathbf{x}} + \sin \phi_{\text{pol}} \hat{\mathbf{y}}, \quad (31)$$

where ϕ_{pol} is the polarization orientation and $\{\hat{\mathbf{x}}, \hat{\mathbf{y}}\}$ are transverse Cartesian basis vectors. Note that Eq. 31 describes the incoherent electric fields at every point in the back focal plane—it does not describe a coherent plane wave. To find the electric field immediately after the paraxial lens we apply a position-dependent rotation matrix (see the rotation matrices in [1, 8] under the paraxial approximation)

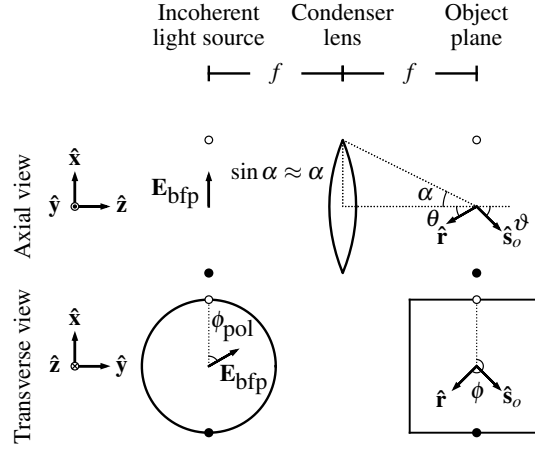


Fig. 3. Illumination geometry and coordinates. We calculate the excitation kernel $h_{\text{exc}}(\hat{\mathbf{s}}_o)$ for a paraxial, unpolarized, incoherent light source (or its image) in the back focal plane of the condenser lens.

$$\mathbf{E}_{\text{ff}}(\theta, \phi, \phi_{\text{pol}}) \propto \begin{bmatrix} 1 & 0 & \theta \cos \phi \\ 0 & 1 & \theta \sin \phi \\ -\theta \cos \phi & -\theta \sin \phi & 1 \end{bmatrix} \begin{bmatrix} \cos \phi_{\text{pol}} \\ \sin \phi_{\text{pol}} \\ 0 \end{bmatrix} \quad (32)$$

$$\mathbf{E}_{\text{ff}}(\theta, \phi, \phi_{\text{pol}}) \propto \cos \phi_{\text{pol}} \hat{\mathbf{x}} + \sin \phi_{\text{pol}} \hat{\mathbf{y}} - \theta \cos(\phi - \phi_{\text{pol}}) \hat{\mathbf{z}}. \quad (33)$$

The probability that a dipole oriented along $\hat{\mathbf{s}}_o$ is excited by a ray with electric field \mathbf{E} is given by

$$|\mathbf{E}_{\text{ff}}(\theta, \phi, \phi_{\text{pol}}) \cdot \hat{\mathbf{s}}_o|^2 \propto s_x^2 \cos^2 \phi_{\text{pol}} + s_y^2 \sin^2 \phi_{\text{pol}} + s_z^2 \theta^2 \cos^2(\phi - \phi_{\text{pol}}). \quad (34)$$

To find the complete excitation kernel we need to integrate Eq. 34 over all polarization orientations and rays

$$h_{\text{exc}}(\hat{\mathbf{s}}_o) \propto \int_0^\alpha \theta d\theta \int_0^{2\pi} d\phi \int_0^{2\pi} d\phi_{\text{pol}} |\mathbf{E}_{\text{ff}}(\theta, \phi, \phi_{\text{pol}}) \cdot \hat{\mathbf{s}}_o|^2, \quad (35)$$

where α is the maximum angle the illumination rays make with the optical axis. Plugging Eq. 34 into Eq. 35, evaluating the integrals, and dropping constants gives

$$h_{\text{exc}}(\vartheta) \propto s_x^2 + s_y^2 + \frac{1}{2} \alpha^2 s_z^2. \quad (36)$$

We can rewrite the excitation kernel in terms of a single variable with the substitutions $s_x^2 + s_y^2 = \sin^2 \vartheta$ and $s_z^2 = \cos^2 \vartheta$

$$h_{\text{exc}}(\vartheta) \propto \sin^2 \vartheta + \frac{1}{2} \alpha^2 \cos^2 \vartheta. \quad (37)$$

Figure 4 shows the excitation kernel as a function of inclination angle ϑ and maximum excitation angle α . The largest variation of the excitation kernel occurs when the maximum excitation angle is zero—plane-wave illumination. As α grows dipoles parallel to the optic axis are more likely to be excited and the variation of the excitation kernel decreases. Note that we have derived this simple model under the paraxial approximation, so it does not make quantitative predictions for high-NA illumination geometries.

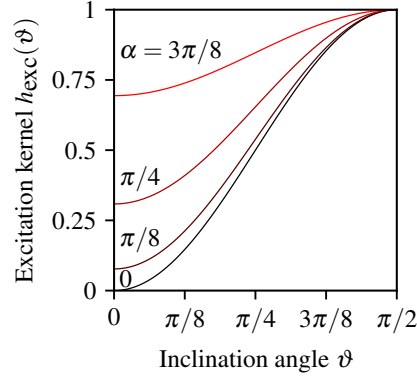


Fig. 4. Dipole excitation kernel $h_{\text{exc}}(\vartheta)$ as a function of inclination angle ϑ and maximum excitation angle α .

2.3.4. Dipole detection model

In this section we will calculate the detection kernel of an epi-detection microscope—the irradiance on the detector due to a single dipole with fixed position and orientation. Our approach mimics existing work [1, 9, 10], but we restrict ourselves to the paraxial approximation.

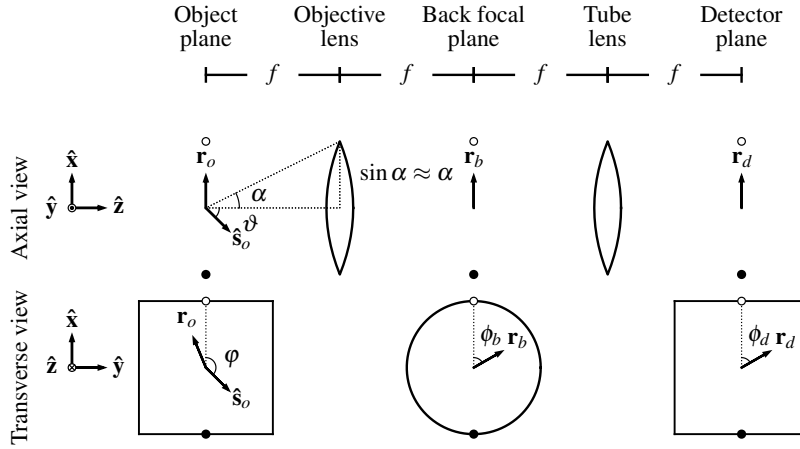


Fig. 5. Detection geometry and coordinates. We calculate the detection kernel $h_{\text{det}}(\mathbf{r}_d, \mathbf{r}_o, \hat{\mathbf{s}}_o)$ for a paraxial $4f$ imaging system.

We consider a single dipole emitter at the origin with a fixed dipole emission moment oriented along $\hat{\mathbf{s}}_o$. The electric field at a position \mathbf{r} far from the dipole is given by

$$\mathbf{E}_{\text{ff}}(\mathbf{r}, \hat{\mathbf{s}}_o) \propto \frac{\exp[ik|\hat{\mathbf{r}}|]}{|\hat{\mathbf{r}}|} \hat{\mathbf{r}} \times \hat{\mathbf{s}}_o \times \hat{\mathbf{r}}. \quad (38)$$

We place the dipole in the focal plane of the same $4f$ imaging system we considered in the monopole case—see Figure 5. The dipole emits spherical wavefronts so we can reuse our argument for shift invariance and drop the phase dependence of the electric field

$$\mathbf{E}_{\text{ff}}(\mathbf{r}, \hat{\mathbf{s}}_o) \propto \hat{\mathbf{r}} \times \hat{\mathbf{s}}_o \times \hat{\mathbf{r}} \quad (39)$$

We also note that we can rewrite a shift-invariant kernel as

$$h_{\text{det}}(\mathbf{r}_d, \mathbf{r}_o, \hat{\mathbf{s}}_o) = h_{\text{det}}(\mathbf{r}_d - \mathbf{r}_o, \hat{\mathbf{s}}_o), \quad (40)$$

which will simplify our derivation—we only need to calculate the response for a dipole positioned along the optic axis. We can rewrite the cross products in terms of a matrix multiplication

$$\mathbf{E}_{\text{ff}}(\mathbf{r}, \hat{\mathbf{s}}_o) \propto [\mathbf{I} - \hat{\mathbf{r}}\hat{\mathbf{r}}^\dagger]\hat{\mathbf{s}}_o, \quad (41)$$

where \mathbf{I} is a 3×3 identity matrix. If we place the molecule in the focal plane of an aplanatic and polarization-preserving objective lens with its optical axis aligned with the $\hat{\mathbf{z}}$ axis (or reuse the illumination objective), then we can find the electric field in the back focal plane by multiplying the electric field with a position-dependent rotation matrix and truncating waves outside the detection collection angle α

$$\mathbf{E}_{\text{bfp}}(\mathbf{r}, \hat{\mathbf{s}}_o) \propto \mathbf{R}_{\text{obj}}(\hat{\mathbf{r}})[\mathbf{I} - \hat{\mathbf{r}}\hat{\mathbf{r}}^\dagger]\hat{\mathbf{s}}_o \Pi\left(\frac{\theta}{\alpha}\right). \quad (42)$$

After plugging in paraxial positions

$$\hat{\mathbf{r}}(\theta, \phi) \approx \theta \cos \phi \hat{\mathbf{x}} + \theta \sin \phi \hat{\mathbf{y}} + \hat{\mathbf{z}}, \quad (43)$$

and the paraxial rotation matrix

$$\mathbf{R}_{\text{obj}}(\theta, \phi) = \begin{bmatrix} 1 & 0 & -\theta \cos \phi \\ 0 & 1 & -\theta \sin \phi \\ -\theta \cos \phi & -\theta \sin \phi & 1 \end{bmatrix}, \quad (44)$$

then dropping the $\theta^2 \hat{\mathbf{z}}$ components and changing from spherical coordinates to cylindrical coordinates by substituting (r_b, ϕ_b) for (θ, ϕ) we find that

$$\mathbf{E}_{\text{bfp}}(r_b, \phi_b, \hat{\mathbf{s}}_o) \propto \{[s_x - s_z r_b \cos \phi_b] \hat{\mathbf{x}} + [s_y - s_z r_b \sin \phi_b] \hat{\mathbf{y}}\} \Pi\left(\frac{r_b}{\alpha}\right). \quad (45)$$

Equation 45 is easier to work with if we introduce the radial vector field $\hat{\boldsymbol{\rho}} = \cos \phi_b \hat{\mathbf{x}} + \sin \phi_b \hat{\mathbf{y}}$ and rewrite as

$$\mathbf{E}_{\text{bfp}}(r_b, \phi_b, \hat{\mathbf{s}}_o) \propto \{s_x \hat{\mathbf{x}} + s_y \hat{\mathbf{y}} - s_z r_b \hat{\boldsymbol{\rho}}\} \Pi\left(\frac{r_b}{\alpha}\right). \quad (46)$$

Equation 46 shows that the transverse components of the dipole (s_x, s_y) create linear vector fields in the back focal plane ($\hat{\mathbf{x}}, \hat{\mathbf{y}}$) while the axial component of the dipole s_z creates a radial vector field in the back focal plane $\hat{\mathbf{z}}$.

We complete the $4f$ system by placing a tube lens one focal length from the back focal plane and a planar detector—see Figure 5. Under the paraxial approximation we can find the electric field in the detector plane by taking the Fourier transform of the field in the back focal plane [11]

$$\mathbf{E}_{\text{det}}(\mathbf{r}_d, \hat{\mathbf{s}}_o) = \int_{\mathbb{R}^2} d\mathbf{r}_b \mathbf{E}_{\text{bfp}}(\mathbf{r}_b) \exp[ik \mathbf{r}_b \cdot \mathbf{r}_d]. \quad (47)$$

We evaluate the integral in Appendix A and show that

$$\mathbf{E}_{\text{det}}(r_d, \hat{\mathbf{s}}_o) \propto \frac{J_1(k\alpha r_d)}{k\alpha r_d} s_x \hat{\mathbf{x}} + \frac{J_1(k\alpha r_d)}{k\alpha r_d} s_y \hat{\mathbf{y}} - i\alpha \frac{J_2(k\alpha r_d)}{k\alpha r_d} s_z \hat{\boldsymbol{\rho}}. \quad (48)$$

Once again we find that the transverse component of the dipole creates a linear field and the axial component of the dipole creates a radial field, but on the detector the linear and radial fields are out of phase by $\pi/2$. This crucial phase factor is a direct consequence of the fact that the linear fields are real and even—the Fourier transform of a real and even function is real and even—and the radial fields are real and odd—the Fourier transform of a real and odd function is imaginary and odd.

Our final step is to calculate the irradiance on the detector

$$h_{\text{det}}(r_d, \hat{\mathbf{s}}_o) \propto |\mathbf{E}_{\text{det}}(r_d, \hat{\mathbf{s}}_o)|^2. \quad (49)$$

The irradiance is the sum of the contributions from the linear and radial fields since their fields are out of phase, so

$$h_{\text{det}}(r_d, \vartheta) \propto a_1(r_d) \sin^2 \vartheta + \frac{1}{2} \alpha^2 a_2(r_d) \cos^2 \vartheta, \quad (50)$$

where we have defined

$$a_n(r_d) \equiv \frac{n}{\pi} \left[\frac{J_n(k\alpha r_d)}{k\alpha r_d} \right]^2. \quad (51)$$

Notice that we retain the α^2 irradiance term even though we dropped θ^2 electric field terms since these terms would become θ^2 irradiance terms.

Figures 6 and 7 summarize the most important features of the dipole detection model. When α is very small the detection kernel is the usual Airy pattern weighted by $\sin^2 \vartheta$. Note that the monopole detection model ignores the $\sin^2 \vartheta$ dependence—see Figure 7 a) and b). As α grows the relative contribution of the higher-order Airy pattern increases. The most important result is that the dipole detection model is not separable into the product of a spatial and angular kernel—even under the paraxial approximation. The detection model is only separable when α approaches zero which is almost never the case in real microscopes. We refer to the non-separability of the detection kernel as *spatio-angular coupling* because the orientation of the dipole is coupled to the spatial pattern of irradiance on the detector.

The paraxial detection kernel is rotationally symmetric—it depends on r_d instead of \mathbf{r}_d . This symmetry is a result of the $\pi/2$ phase shift between the linear and radial fields on the detector. If the phase shift between the linear and radial fields was not exactly $\pi/2$ then the fields would interfere on the detector, and we would lose rotational symmetry. Tracing back further, the rotational symmetry is due to the fact that the field in the back focal plane could be written as a sum of a linear and radial field which is only true under the paraxial approximation—the rotational symmetry of the detection kernel is only true to first order. Despite the approximation, we still feel that the rotational symmetry of the detection kernel is a valuable result since it helps build an intuition about the dominant effects outside the paraxial approximation. Later in this work we will exploit this approximate symmetry to improve the efficiency of simulating and inverting the imaging model.

Note that we have restricted our analysis to an imaging system with unit magnification. We will continue with this simplification and mention that an imaging system with an arbitrary magnification can be modeled using the model for a system with unit magnification and a change of variable (see [5] section 7.2.7).

2.3.5. Simplified dipole imaging model

Combining the results of the previous two sections yields a simplified dipole imaging model

$$g(\mathbf{r}_d) = \int_{\mathbb{S}^2} d\hat{\mathbf{s}}_o \int_{\mathbb{R}^2} d\mathbf{r}_o h(|\mathbf{r}_d - \mathbf{r}_o|, |\hat{\mathbf{s}}_o \cdot \hat{\mathbf{z}}|) f(\mathbf{r}_o, \hat{\mathbf{s}}_o). \quad (52)$$

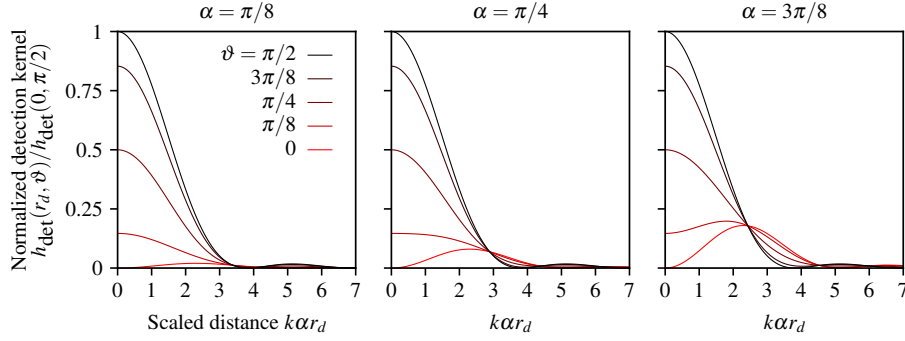


Fig. 6. Normalized detection kernel as a function of the scaled radial detection coordinate $k\alpha r_d$, the dipole inclination angle ϑ , and the collection angle α . For small collection angles (left) the detection kernel of axial dipoles (**red**) is small compared to transverse dipoles (**black**), but the relative contribution of axial dipoles increases with the collection angle (see **red** lines from left to right).

where we have written the kernel in terms of $|\hat{\mathbf{s}}_o \cdot \hat{\mathbf{z}}| = \cos \vartheta$ to explicitly show the dependence on $\hat{\mathbf{s}}_o$. In previous sections we showed that the kernel is given by

$$h(r, \vartheta) \propto h_{\text{exc}}(\vartheta) h_{\text{det}}(r, \vartheta). \quad (53)$$

Plugging in our results

$$h(r, \vartheta) \propto \left[\sin^2 \vartheta + \frac{1}{2} \alpha^2 \cos^2 \vartheta \right] \left[a_1(r) \sin^2 \vartheta + \frac{1}{2} \alpha^2 a_2(r) \cos^2 \vartheta \right]. \quad (54)$$

2.3.6. Orientation-dependent optical transfer function

In Appendix C we evaluate the 2D spatial Fourier transforms of $a_1(r)$ and $a_2(r)$ to find that

$$H(\nu, \vartheta) \propto \left[\sin^2 \vartheta + \frac{1}{2} \alpha^2 \cos^2 \vartheta \right] \left[A_1(\nu) \sin^2 \vartheta + \frac{1}{2} \alpha^2 A_2(\nu) \cos^2 \vartheta \right]. \quad (55)$$

where

$$A_1(\nu) = \frac{2}{\pi} \left\{ \cos^{-1} \left(\frac{\nu}{2\nu_o} \right) - \frac{\nu}{2\nu_o} \sqrt{1 - \left(\frac{\nu}{2\nu_o} \right)^2} \right\} \Pi \left(\frac{\nu}{2\nu_o} \right), \quad (56)$$

$$A_2(\nu) = \frac{2}{\pi} \left\{ \cos^{-1} \left(\frac{\nu}{2\nu_o} \right) - \left[3 - 2 \left(\frac{\nu}{2\nu_o} \right)^2 \right] \frac{\nu}{2\nu_o} \sqrt{1 - \left(\frac{\nu}{2\nu_o} \right)^2} \right\} \Pi \left(\frac{\nu}{2\nu_o} \right). \quad (57)$$

The STF is shown in Figure 8. The STF has the usual spatial-frequency cutoff at $\nu = 2\nu_o$ for all dipole orientations.

2.3.7. Angular transfer function (ATF)

To calculate the angular transfer function we plug the spatio-angular point spread function Eq. 54 into Eq. 18 and evaluate the integrals using a computer algebra package [12] to find

$$\begin{aligned} H_l^m(r) \propto & 7 \{ 32a_1(r) + 4\alpha^2[a_1(r) + a_2(r)] + 3\alpha^4 a_2(r) \} \delta_{\ell 0} \delta_{m 0} + \\ & 4\sqrt{5} \{ -16a_1(r) + \alpha^2[a_1(r) + a_2(r)] + 3\alpha^4 a_2(r) \} \delta_{\ell 2} \delta_{m 0} + \\ & 8 \{ 4a_1(r) - 2\alpha^2[a_1(r) + a_2(r)] + \alpha^4 a_2(r) \} \delta_{\ell 4} \delta_{m 0}. \end{aligned} \quad (58)$$

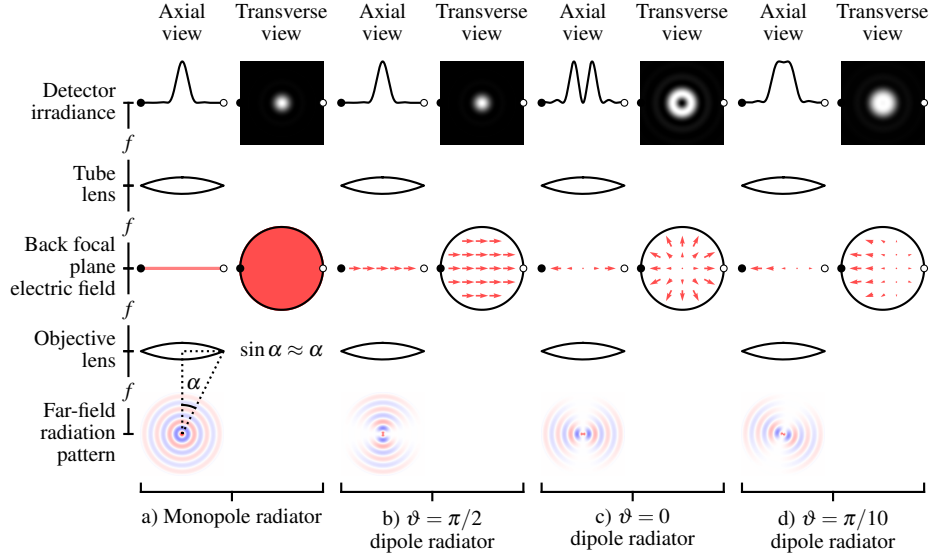


Fig. 7. Comparison of paraxial detection models for monopole radiators a) and dipole radiators b)–d). a) Monopole radiators fill the back focal plane with a uniform scalar field which gives rise to the familiar Airy disk on the detector. b) A transverse dipole radiator also creates an Airy disk, but the back focal plane is filled with a uniform vector field. c) An axial dipole radiator creates a radial electric field pattern in the back focal plane which creates a higher-order Airy disk on the detector. d) Dipoles that are not transverse or axial still create radially symmetric irradiance patterns under the paraxial approximation. Fields from transverse dipoles are real and even while fields from axial dipoles are real and odd which causes a relative $\pi/2$ phase shift for the fields on the detector. This phase shift means that the fields from transverse and axial components of the dipole do not interfere which causes radially symmetric irradiance patterns.

The degree ℓ and order m of the non-zero terms in the ATF follow directly from specific features of the kernel. First, our kernel is symmetric under inversion of the dipole moment which appears in the kernel as even-degreed trigonometric functions. This symmetry is maintained in the ATF since all of the non-zero terms have an even degree $\ell = 0, 2$, and 4 . Second, we showed that under the paraxial approximation our kernel is rotationally symmetric which allows us to write the kernel as a function of r instead of \mathbf{r} . This symmetry is maintained in the ATF since all of the non-zero terms have order $m = 0$. Finally, both the excitation and detection kernels are a weighted sum of degree-2 trigonometric functions which implies that the maximum degree of the kernel is 4. This feature of the kernel appears in the ATF since only $\ell = 0, 2$, and 4 terms are non-zero.

2.3.8. Spatio-angular transfer function (SATF)

$$\begin{aligned}
 H_{\ell}^m(\nu) \propto & 7\{ 32A_1(\nu) + 4\alpha^2[A_1(\nu) + A_2(\nu)] + 3\alpha^4A_2(\nu)\}\delta_{\ell 0}\delta_{m 0} + \\
 & 4\sqrt{5}\{-16A_1(\nu) + \alpha^2[A_1(\nu) + A_2(\nu)] + 3\alpha^4A_2(\nu)\}\delta_{\ell 2}\delta_{m 0} + \\
 & 8\{ 4A_1(\nu) - 2\alpha^2[A_1(\nu) + A_2(\nu)] + \alpha^4A_2(\nu)\}\delta_{\ell 4}\delta_{m 0}.
 \end{aligned} \tag{59}$$

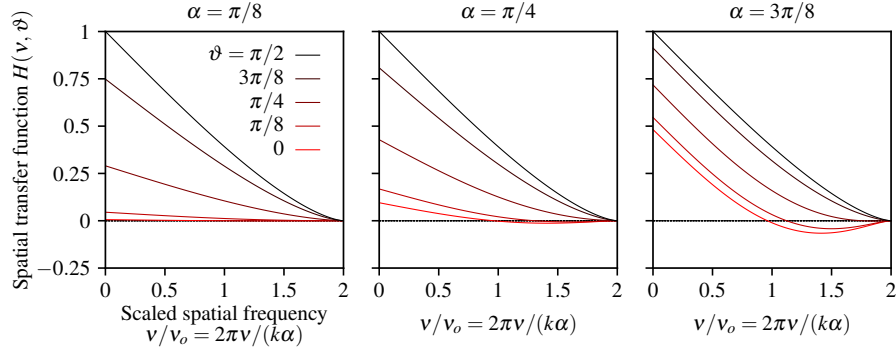


Fig. 8. STF as a function of the scaled spatial frequency, the dipole inclination angle ϑ , and the collection angle α . For small collection angles (left) the STF for axial dipoles (**red**) is small compared to transverse dipoles (**black**), but the relative contribution of axial dipoles increases with the collection angle (see **red** lines from left to right). The STF of axial dipoles is negative at high spatial frequencies because the central minimum of the axial kernel corresponds to the position of the dipole. Equivalently, a high-spatial-frequency pattern of axial dipoles will generate an irradiance pattern where the minimum irradiance corresponds to the peak of the axial dipole density.

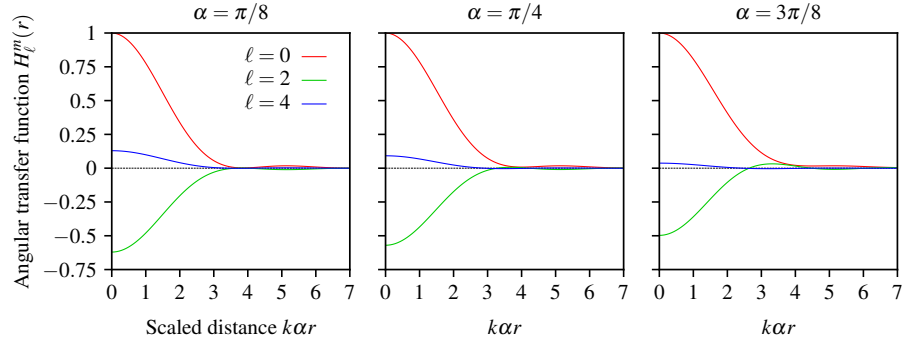


Fig. 9. ATF as a function of the scaled radial detection coordinate $k\alpha r$, the spherical harmonic degree ℓ , and the collection angle α .

3. Results

- 3.1. Phantom with spatio-angular sparsity (single molecules)
- 3.2. Phantom with spatial sparsity (rotating single molecules)
- 3.3. Phantom with angular sparsity (actin fibers)
- 3.4. Phantom without sparsity (most general)

4. Discussion **Very rough but open for discussion**

4.1. Reconstructions

Since the ATF effectively contains three OTFs it is tempting to conclude that fluorescence microscopes pass three times as much information about the dipoles as monopoles. This is not true. The microscope still only measures a single member of $\mathbb{L}_2(\mathbb{R}^2)$ so at best we can recover the same amount of information about the object. In other words, we know immediately that the

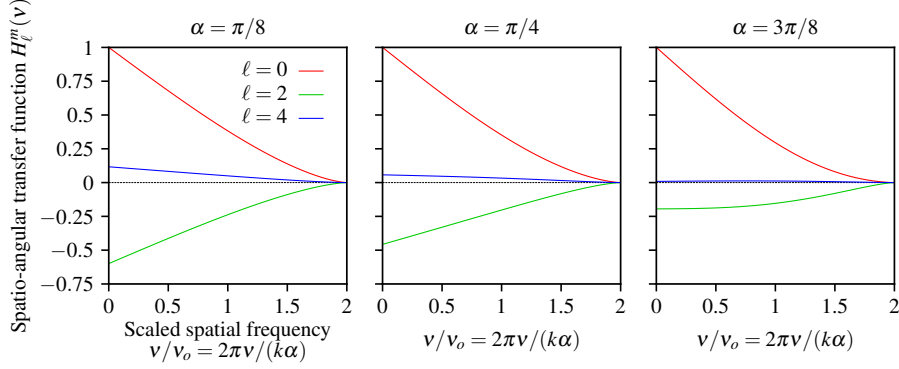


Fig. 10. SATF as a function of the scaled spatial frequency, the spherical harmonic degree ℓ , and the collection angle α .

microscope is a rank-1 operator since it only measures one continuous function.

We postpone a full discussion of SVD to find the object space singular functions that span the measurement space of the instrument.

4.2. Alternative transfer functions

Throughout this work we have used the spherical harmonic functions as a basis for functions on the sphere, but there are other basis functions that can be advantageous in some cases. Backer and others [CITE TODO] have used the second moments as basis functions for the sphere because they arise naturally when computing the spatio-angular point spread function. Mathematically, Backer and Lew use an alternative to the angular transfer function that uses the second moments as basis functions so their forward model is given by

$$g(\mathbf{r}_d) = \sum_{j=1}^6 H_j(\mathbf{r}_d - \mathbf{r}_o) F_j(\mathbf{r}_o) \quad (60)$$

where

$$H_j(\mathbf{r}_d - \mathbf{r}_o) = \int_{\mathbb{S}^2} d\hat{\mathbf{s}}_o h(\mathbf{r}_d - \mathbf{r}_o, \hat{\mathbf{s}}_o) Z_j(\hat{\mathbf{s}}_o), \quad (61)$$

$$F_j(\mathbf{r}_o) = \int_{\mathbb{S}^2} d\hat{\mathbf{s}}_o f(\mathbf{r}_o, \hat{\mathbf{s}}_o) Z_j(\hat{\mathbf{s}}_o), \quad (62)$$

and $Z_j(\hat{\mathbf{s}}) = \{s_x^2, s_y^2, s_z^2, s_x s_y, s_y s_z, s_x s_z\}$ are the second moments. This formulation provides the main advantage of the ATF approach—efficient computation for spatially sparse and angularly dense samples—without requiring a cumbersome expansion of the spatio-angular point spread function onto spherical harmonics.

The spherical harmonics provide several advantages over the second moments as well. First, the spherical harmonics form an orthonormal basis which often simplifies computation. For example, if we calculated the angular detection transfer function we would find that it contained two angular terms under the paraxial approximation. If we expanded onto second moments we would need all six angular basis functions and computing the forward model would be three times as expensive. Second, the spherical harmonics are complete which means they can represent arbitrary functions on the sphere while the second moments can only represent a small subset of all functions on the sphere. Extending the accuracy of the second moments using the fourth

(or higher) moments is possible, but it requires a completely new basis. Indeed, the simple microscope we consider in this work requires an expansion onto fourth-order spherical harmonics, so an expansion onto second-order moments would not suffice. Finally, using the spherical harmonics provides access to a set of fast algorithms. The naive expansion of an arbitrary discretized N point spherical function onto spherical harmonics (or second moments) requires a $O(N^2)$ matrix multiplication while pioneering work by Driscoll and Healy [cite] showed that the forward discrete fast spherical harmonic transform can be computed with a $O(N(\log N)^2)$ algorithm and its inverse can be computed with a $O(N^{3/2})$ algorithm. To our knowledge no similarly fast algorithms exist for expansion onto the higher-order moments.

The diffusion magnetic resonance imaging uses both sets of bases [cite Bassar] [cite Tournier] for particular cases.

4.3. What determines the angular frequency cutoff?

The spatial-frequency cutoff of a fluorescence microscope is well known to vary as NA/λ —we can increase spatial resolution by increasing the NA of the instrument or by choosing a fluorophore with a shorter emission wavelength. Analogously, the angular-frequency spectrum of a fluorescence microscope depends on both the instrument and the sample.

The simple paraxial microscope considered in this work always has three terms in its angular-frequency spectrum, but we can increase the number of terms by modifying the instrument. We will postpone the proper treatment of these effects until future work, but we briefly mention that the number of terms in the angular-frequency spectrum increases for non-paraxial microscopes, microscopes with polarizers on the illumination or detection paths, and multiview microscopes. We also mention that there are two ways to extend the angular-frequency spectrum of a microscope—by increasing the degree ℓ and by increasing the order m . Extending the angular degree cutoff ℓ_0 gives the microscope the ability to measure finer angular features, while extending the angular order cutoff m_0 give the microscope the ability to measure features of the object that are increasingly invariant to rotation. If the angular order cutoff matches the angular degree cutoff $\ell_0 = m_0$ then the microscope can be said to have *isotropic angular resolution*. This condition is not met by a single-view paraxial microscope since $\ell_0 = 4$ and $m_0 = 0$, but we will model microscopes with this property in future work.

The number of terms in the angular frequency spectrum is also sample dependent. Monopoles emit light isotropically so they have a single term, dipoles have a three-term ATF, and higher-order excitation and detection moments will have even more terms—these objects have different angular band limits. We emphasize the similarity between the spatial and angular frequency cutoffs—both the sample and the instrument affect the maximum achievable resolution of the imaging system.

Possibly implies that the spatio-angular transfer function can be factored. Cite 3D vector transfer functions Arnison and Sheppard.

4.4. Characterizing real spatio-angular microscopes

The theoretical model we present in this work is an extreme simplification of a real microscope. We have ignored the effects of thick samples, optical aberration, scattering, high-NA objectives, finite fluorescence lifetimes, and interactions between fluorophores, and we are sure that this list of limitations could be extended. Because of this long list of unknown effects, real experiments should make an attempt to characterize the specific imaging system.

Typical fluorescence microscopy experiments start with the monopole approximation and attempt to characterize the microscope by imaging sub-diffraction beads. These images are assumed to be good approximations of the monopole point spread function and this data can be used to restore (deconvolve) the data taken in arbitrary experiments.

Imaging sub-diffraction beads is not enough to completely characterize the response of a microscope to an oriented sample. We need at least three samples with a known orientations to

characterize the SATF, so isotropic beads are not enough. Small beads may not be isotropic [cite Lew].

5. Conclusion

Most models of fluorescence microscopes use a monopole model to describe the object and the imaging system. A more complete description of any fluorescence microscope requires a dipole model of the object and a model of the spatio-angular point spread function. We developed several transfer functions that simplify the mapping between the spatio-angular density and the irradiance pattern on the detector, and we demonstrated these transfer functions by efficiently simulating a paraxial widefield fluorescence microscope.

References

1. A. S. Backer and W. E. Moerner, “Extending single-molecule microscopy using optical Fourier processing,” *J. Phys. Chem. B* **118**, 8313–8329 (2014).
2. M. A. Lieb, J. M. Zavislan, and L. Novotny, “Single-molecule orientations determined by direct emission pattern imaging,” *J. Opt. Soc. Am. B* **21**, 1210–1215 (2004).
3. M. P. Backlund, M. D. Lew, A. S. Backer, S. J. Sahl, and W. E. Moerner, “The role of molecular dipole orientation in single-molecule fluorescence microscopy and implications for super-resolution imaging,” *ChemPhysChem* **15**, 587–599 (2014).
4. S. B. Mehta, M. McQuilken, P. J. La Rivière, P. Occhipinti, A. Verma, R. Oldenbourg, A. S. Gladfelter, and T. Tani, “Dissection of molecular assembly dynamics by tracking orientation and position of single molecules in live cells,” *Proc. Natl. Acad. Sci. U.S.A.* **113**, E6352–E6361 (2016).
5. H. Barrett and K. Myers, *Foundations of image science*, Wiley series in pure and applied optics (Wiley-Interscience, 2004).
6. J. T. Fourkas, “Rapid determination of the three-dimensional orientation of single molecules,” *Opt. Lett.* **26**, 211–213 (2001).
7. T. Chandler, S. Mehta, H. Shroff, R. Oldenbourg, and P. J. La Rivière, “Single-fluorophore orientation determination with multiview polarized illumination: modeling and microscope design,” *Opt. Express* **25**, 31309–31325 (2017).
8. M. R. Foreman and P. Török, “Computational methods in vectorial imaging,” *J. Mod. Opt.* **58**, 339–364 (2011).
9. L. Novotny and B. Hecht, *Principles of Nano-Optics* (Cambridge University Press, 2006).
10. A. Agrawal, S. Quirin, G. Grover, and R. Piestun, “Limits of 3D dipole localization and orientation estimation for single-molecule imaging: towards Green’s tensor engineering,” *Opt. Express* **20**, 26667–26680 (2012).
11. J. Goodman, *Introduction to Fourier Optics* (McGraw-Hill, 1996), 2nd ed.
12. A. Meurer, C. P. Smith, M. Paprocki, O. Čertík, S. B. Kirpichev, M. Rocklin, A. Kumar, S. Ivanov, J. K. Moore, S. Singh, T. Rathnayake, S. Vig, B. E. Granger, R. P. Muller, F. Bonazzi, H. Gupta, S. Vats, F. Johansson, F. Pedregosa, M. J. Curry, A. R. Terrel, v. Roučka, A. Saboo, I. Fernando, S. Kulal, R. Cimrman, and A. Scopatz, “SymPy: symbolic computing in Python,” *PeerJ Comput. Sci.* **3**, e103 (2017).
13. N. Schaeffer, “Efficient spherical harmonic transforms aimed at pseudospectral numerical simulations,” *Geochem. Geophys. Geosystems* **14**, 751–758 (2013).
14. J. Mertz, *Introduction to Optical Microscopy* (W. H. Freeman, 2009).
15. A. Poularikas, *Handbook of Formulas and Tables for Signal Processing*, Electrical Engineering Handbook (CRC-Press, 1998).

A. Fourier transform of linear and radial vector fields

$$\mathbf{E}_{\text{det}}(\mathbf{r}_d, \hat{\mathbf{s}}_o) = \int_{\mathbb{R}^2} d\mathbf{r}_b \mathbf{E}_{\text{bfp}}(\mathbf{r}_b) \exp[ik \mathbf{r}_b \cdot \mathbf{r}_d]. \quad (63)$$

To evaluate the integral we rewrite it in polar coordinates

$$\mathbf{E}_{\text{det}}(\mathbf{r}_d, \hat{\mathbf{s}}_o) = \int_0^\alpha r_b dr_b \int_0^{2\pi} d\phi_b \mathbf{E}_{\text{bfp}}(r_b, \phi_b) \exp[ikr_b r_d \cos(\phi_b - \phi_d)], \quad (64)$$

plug in Eq. 45, and apply the following identities

$$\int_0^{2\pi} d\phi_b \begin{Bmatrix} \sin(n\phi_b) \\ \cos(n\phi_b) \end{Bmatrix} \exp[ikr_b r_d \cos(\phi_b - \phi_d)] = 2\pi i^n \begin{Bmatrix} \sin(n\phi'_o) \\ \cos(n\phi'_o) \end{Bmatrix} J_n(kr_b r_d), \quad (65)$$

$$\int_0^\alpha dr_b (r_b)^{n+1} J_n(kr_b r_d) = \alpha^{n+1} \left[\frac{J_{n+1}(k\alpha r_d)}{k\alpha r_d} \right], \quad (66)$$

to find that

$$\begin{aligned} \mathbf{E}_{\text{det}}(\mathbf{r}_d, \hat{\mathbf{s}}_o) \propto & \left[s_x \frac{J_1(k\alpha r_d)}{k\alpha r_d} - i s_z \alpha \frac{J_2(k\alpha r_d)}{k\alpha r_d} \cos \phi_d \right] \hat{\mathbf{x}} + \\ & \left[s_y \frac{J_1(k\alpha r_d)}{k\alpha r_d} - i s_z \alpha \frac{J_2(k\alpha r_d)}{k\alpha r_d} \sin \phi_d \right] \hat{\mathbf{y}}. \end{aligned} \quad (67)$$

Similar to the back focal plane, we rewrite in terms of linear and radial vector fields

$$\mathbf{E}_{\text{det}}(\mathbf{r}_d, \hat{\mathbf{s}}_o) \propto \frac{J_1(k\alpha r_d)}{k\alpha r_d} [s_x \hat{\mathbf{x}} + s_y \hat{\mathbf{y}}] - i\alpha \frac{J_2(k\alpha r_d)}{k\alpha r_d} s_z \hat{\mathbf{p}}. \quad (68)$$

B. Spherical harmonics

The spherical harmonic function of degree ℓ and order $-\ell \leq m \leq \ell$ is defined as [13]

$$Y_\ell^m(\vartheta, \varphi) = P_\ell^m(\cos \vartheta) \exp(im\varphi) \quad (69)$$

where $P_\ell^m(\cos \theta)$ are the associated Legendre polynomials normalized for the spherical harmonics

$$P_\ell^m(x) = (-1)^m \sqrt{\frac{2\ell+1}{4\pi}} \sqrt{\frac{(\ell-|m|)!}{(\ell+|m|)!}} (1-x^2)^{|m|/2} \frac{d^{|m|}}{dx^{|m|}} P_\ell(x) \quad (70)$$

where $P_\ell(x)$ are the Legendre polynomials defined by the following recurrence

$$P_0(x) = 1, \quad (71)$$

$$P_1(x) = x, \quad (72)$$

$$\ell P_\ell(x) = (2\ell-1)xP_{\ell-1}(x) - (\ell-1)P_{\ell-2}(x). \quad (73)$$

The spherical harmonics are orthonormal which means that

$$\int_{\mathbb{S}^2} d\hat{\mathbf{s}} Y_\ell^m(\hat{\mathbf{s}}) \bar{Y}_{\ell'}^{m'}(\hat{\mathbf{s}}) = \delta_{\ell\ell'} \delta_{mm'}, \quad (74)$$

where $\delta_{\ell\ell'}$ denotes the Kronecker delta. The spherical harmonics form a complete basis so an arbitrary function on the sphere $f(\hat{\mathbf{s}})$ can be expanded into a sum of weighted spherical harmonic functions

$$f(\hat{\mathbf{s}}) = \sum_{\ell=0}^{\infty} \sum_{m=-\ell}^{\ell} F_\ell^m Y_\ell^m(\hat{\mathbf{s}}). \quad (75)$$

We can find the spherical harmonic coefficients F_ℓ^m for a given function by using Fourier's trick—multiply both sides by $\bar{Y}_\ell^m(\hat{\mathbf{s}})$, integrate over the sphere, and exploit orthogonality to find that

$$F_\ell^m = \int_{\mathbb{S}^2} d\hat{\mathbf{s}} f(\hat{\mathbf{s}}) \bar{Y}_\ell^m(\hat{\mathbf{s}}). \quad (76)$$

The coefficients F_ℓ^m are usually called the *spherical Fourier transform* of a spherical function.

We briefly show how two properties of spherical functions propagate to the spherical Fourier transform. First, the spherical harmonic coefficients of spherical functions that can be written entirely as a function of the inclination angle ϑ are zero when $m \neq 0$ because

$$\int_{\mathbb{S}^2} d\hat{\mathbf{s}} f(\vartheta) \bar{Y}_\ell^m(\hat{\mathbf{s}}) = \int_0^{2\pi} d\phi \exp[-im\phi] \int_0^\pi d\vartheta \sin \vartheta f(\vartheta) P_\ell^m(\cos \vartheta), \quad (77)$$

$$= \delta_{m0} \int_0^\pi d\vartheta \sin \vartheta f(\vartheta) P_\ell^m(\cos \vartheta). \quad (78)$$

Second, the spherical harmonic coefficients of spherical functions that are symmetric under inversion $f(\hat{\mathbf{s}}) = f(-\hat{\mathbf{s}})$ are zero when ℓ is odd because $Y_\ell^m(-\hat{\mathbf{s}}_o) = (-1)^\ell Y_\ell^m(\hat{\mathbf{s}})$, so if ℓ is odd then

$$\int_{\mathbb{S}^2} d\hat{\mathbf{s}} f(\hat{\mathbf{s}}) \bar{Y}_{2n+1}^m(\hat{\mathbf{s}}) = \int_{\mathbb{S}^2/2} d\hat{\mathbf{s}} f(+\hat{\mathbf{s}}) \bar{Y}_{2n+1}^m(+\hat{\mathbf{s}}) + \int_{\mathbb{S}^2/2} d\hat{\mathbf{s}} f(-\hat{\mathbf{s}}) \bar{Y}_{2n+1}^m(-\hat{\mathbf{s}}), \quad (79)$$

$$= \int_{\mathbb{S}^2/2} d\hat{\mathbf{s}} f(\hat{\mathbf{s}}) \bar{Y}_{2n+1}^m(+\hat{\mathbf{s}}) - \int_{\mathbb{S}^2/2} d\hat{\mathbf{s}} f(\hat{\mathbf{s}}) \bar{Y}_{2n+1}^m(\hat{\mathbf{s}}) = 0. \quad (80)$$

C. Fourier transform of first and second order Airy patterns

$$a_n(r_d) \equiv \frac{n}{\pi} \left[\frac{J_n(k\alpha r_d)}{k\alpha r_d} \right]^2. \quad (81)$$

$$A_n(\nu) \equiv \mathcal{F}_2\{a_n(r_o)\} = \int_{\mathbb{R}^2} d\mathbf{r}_o \exp[i2\pi\mathbf{r}_o \cdot \boldsymbol{\nu}] a_n(r_d), \quad (82)$$

Our final task is to calculate $A_1(\nu)$ and $A_2(\nu)$. $A_1(\nu)$ is a well-known result [11, 14], but we review the calculation to establish the tools we'll need to evaluate $A_2(\nu)$. We start by using the autocorrelation (Wiener-Khinchin) theorem to rewrite the Fourier transform as

$$A_1(\nu) = \frac{1}{\pi} \mathcal{F}_2 \left\{ \left[\frac{J_1(2\pi\nu_o r_o)}{2\pi\nu_o r_o} \right]^2 \right\} = \frac{1}{\pi} \left[\mathcal{F}_2 \left\{ \frac{J_1(2\pi\nu_o r_o)}{2\pi\nu_o r_o} \right\} \star_2 \mathcal{F}_2 \left\{ \frac{J_1(2\pi\nu_o r_o)}{2\pi\nu_o r_o} \right\} \right] \quad (83)$$

where \star_2 denotes a two-dimensional autocorrelation. Next, we recognize that the Fourier transforms on the right hand side of Eq. 83 are rotationally symmetric so they can be rewritten as zero-order Hankel transforms

$$A_1(\nu) = \frac{1}{\pi} \left[\mathcal{H}_0 \left\{ \frac{J_1(2\pi\nu_o r_o)}{2\pi\nu_o r_o} \right\} \star_2 \mathcal{H}_0 \left\{ \frac{J_1(2\pi\nu_o r_o)}{2\pi\nu_o r_o} \right\} \right] \quad (84)$$

We can apply the Hankel transform identity [15]

$$\mathcal{H}_{n-1} \left\{ \frac{J_n(2\pi\nu_o r_o)}{2\pi\nu_o r_o} \right\} = \frac{\nu^{n-1}}{\nu_o^n} \Pi \left(\frac{\nu}{\nu_o} \right), \quad (85)$$

to find that

$$A_1(\nu) = \frac{1}{\pi\nu_o^2} \left[\Pi \left(\frac{\nu}{\nu_o} \right) \star_2 \Pi \left(\frac{\nu}{\nu_o} \right) \right]. \quad (86)$$

We can use the geometric construction in Figure 11 to express the autocorrelation in terms of an integral over a region of overlap between two circles given by

$$A_1(\nu) = \frac{4}{\pi \nu_o^2} \left[\int_0^{\nu_o} \tau d\tau \int_0^{\cos^{-1}\left(\frac{\nu}{2\nu_o}\right)} d\phi_\tau - \int_0^{\nu/2} d\tau_x \int_0^{\tau_x \frac{2\nu_o}{\nu} \sqrt{1-\left(\frac{\nu}{2\nu_o}\right)^2}} d\tau_y \right] \Pi\left(\frac{\nu}{2\nu_o}\right), \quad (87)$$

$$A_1(\nu) = \frac{4}{\pi \nu_o^2} \left[\int_0^{\nu_o} \tau d\tau \cos^{-1}\left(\frac{\nu}{2\nu_o}\right) - \int_0^{\nu/2} d\tau_x \tau_x \frac{2\nu_o}{\nu} \sqrt{1-\left(\frac{\nu}{2\nu_o}\right)^2} \right] \Pi\left(\frac{\nu}{2\nu_o}\right), \quad (88)$$

$$A_1(\nu) = \frac{2}{\pi} \left\{ \cos^{-1}\left(\frac{\nu}{2\nu_o}\right) - \frac{\nu}{2\nu_o} \sqrt{1-\left(\frac{\nu}{2\nu_o}\right)^2} \right\} \Pi\left(\frac{\nu}{2\nu_o}\right). \quad (89)$$

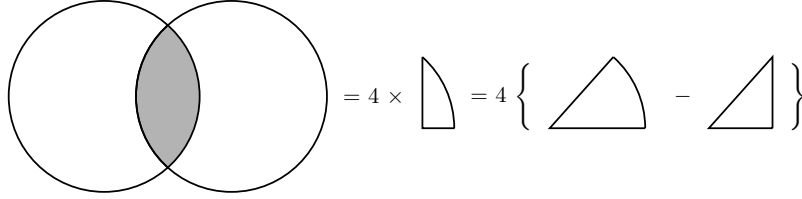


Fig. 11. Geometric construction for evaluating the autocorrelations. We need to integrate over the overlapping region of two circles with radius ν_o and distance ν between their centers. The region is given by four times the difference in area between a sector of angle $\arccos\left(\frac{\nu}{2\nu_o}\right)$ and a triangle with base $\nu/2$ and hypotenuse ν_o .

To evaluate $A_2(\nu)$ we could follow the same steps, but we will reach a dead end because there is no Hankel transform identity for $\mathcal{H}_{n-1}\left\{\frac{J_{n+1}(2\pi\nu_o r_o)}{2\pi\nu_o r_o}\right\}$. Instead, we rewrite $A_2(\nu)$ as

$$A_2(\nu) = \frac{2}{\pi} \mathcal{F}_2 \left\{ \left[\frac{J_2(2\pi\nu_o r_o)}{2\pi\nu_o r_o} \right]^2 \right\} = \frac{2}{\pi} \left[\mathcal{F}_2 \left\{ \left[\frac{J_2(2\pi\nu_o r_o)}{2\pi\nu_o r_o} \cos \phi_\nu \right]^2 \right\} + \mathcal{F}_2 \left\{ \left[\frac{J_2(2\pi\nu_o r_o)}{2\pi\nu_o r_o} \sin \phi_\nu \right]^2 \right\} \right]. \quad (90)$$

Applying the autocorrelation theorem gives

$$A_2(\nu) = \frac{2}{\pi} \left[\mathcal{F}_2 \left\{ \frac{J_2(2\pi\nu_o r_o)}{2\pi\nu_o r_o} \cos \phi_\nu \right\} \star_2 \mathcal{F}_2 \left\{ \frac{J_2(2\pi\nu_o r_o)}{2\pi\nu_o r_o} \cos \phi_\nu \right\} + \mathcal{F}_2 \left\{ \frac{J_2(2\pi\nu_o r_o)}{2\pi\nu_o r_o} \sin \phi_\nu \right\} \star_2 \mathcal{F}_2 \left\{ \frac{J_2(2\pi\nu_o r_o)}{2\pi\nu_o r_o} \sin \phi_\nu \right\} \right]. \quad (91)$$

After converting the Fourier transforms to Hankel transforms with the identities

$$\mathcal{F}_2 \{f(r) \cos(\phi)\} = -i \cos \phi_\nu \mathcal{H}_1 \{f(r)\}, \quad (92)$$

$$\mathcal{F}_2 \{f(r) \sin(\phi)\} = -i \sin \phi_\nu \mathcal{H}_1 \{f(r)\}, \quad (93)$$

and evaluating the Hankel transforms with Eq. 85, we find that

$$A_2(\nu) = -\frac{2}{\pi \nu_o^4} \left\{ \left[\nu_x \Pi\left(\frac{\nu}{\nu_o}\right) \star_2 \nu_x \Pi\left(\frac{\nu}{\nu_o}\right) \right] + \left[\nu_y \Pi\left(\frac{\nu}{\nu_o}\right) \star_2 \nu_y \Pi\left(\frac{\nu}{\nu_o}\right) \right] \right\}. \quad (94)$$

Eq. 94 contains two autocorrelations that require us to find the weighted overlap of two circles. Neither of these autocorrelations are rotationally symmetric, but their sum must be rotationally symmetric. With this symmetry in mind, we recognize that the first autocorrelation is largest for shifts along the x direction and smallest for shifts along the y direction with a smooth $\cos^2 \phi_v$ weighting between the two extremes. The same is true for the second autocorrelations except the x and y axes are exchanged and there is a $\sin^2 \phi_v$ weighting between the two extremes. Therefore, we can rewrite Eq. 94 as

$$A_2(\nu) = -\frac{2}{\pi\nu_o^4} \left\{ \left[\nu_x \Pi \left(\frac{\nu}{\nu_o} \right) \star_2^x \nu_x \Pi \left(\frac{\nu}{\nu_o} \right) \right] \cos^2 \phi_v + \left[\nu_x \Pi \left(\frac{\nu}{\nu_o} \right) \star_2^y \nu_x \Pi \left(\frac{\nu}{\nu_o} \right) \right] \sin^2 \phi_v + \right. \\ \left. \left[\nu_y \Pi \left(\frac{\nu}{\nu_o} \right) \star_2^x \nu_y \Pi \left(\frac{\nu}{\nu_o} \right) \right] \cos^2 \phi_v + \left[\nu_y \Pi \left(\frac{\nu}{\nu_o} \right) \star_2^y \nu_y \Pi \left(\frac{\nu}{\nu_o} \right) \right] \sin^2 \phi_v \right\}. \quad (95)$$

where \star_2^x denotes a two-dimensional autocorrelation for shifts along the x direction. We can use the following pair of identities

$$\nu_x \Pi \left(\frac{\nu}{\nu_o} \right) \star_2^x \nu_x \Pi \left(\frac{\nu}{\nu_o} \right) = \nu_y \Pi \left(\frac{\nu}{\nu_o} \right) \star_2^y \nu_y \Pi \left(\frac{\nu}{\nu_o} \right), \quad (96)$$

$$\nu_x \Pi \left(\frac{\nu}{\nu_o} \right) \star_2^y \nu_x \Pi \left(\frac{\nu}{\nu_o} \right) = \nu_y \Pi \left(\frac{\nu}{\nu_o} \right) \star_2^x \nu_y \Pi \left(\frac{\nu}{\nu_o} \right), \quad (97)$$

to simplify Eq. 95 to

$$A_2(\nu) = -\frac{2}{\pi\nu_o^4} \left\{ \left[\nu_x \Pi \left(\frac{\nu}{\nu_o} \right) \star_2^x \nu_x \Pi \left(\frac{\nu}{\nu_o} \right) \right] + \left[\nu_x \Pi \left(\frac{\nu}{\nu_o} \right) \star_2^y \nu_x \Pi \left(\frac{\nu}{\nu_o} \right) \right] \right\}. \quad (98)$$

First we evaluate the autocorrelation for shifts along the x axis

$$= -\frac{2}{\pi\nu_o^4} \left[\nu_x \Pi \left(\frac{\nu}{\nu_o} \right) \star_2^x \nu_x \Pi \left(\frac{\nu}{\nu_o} \right) \right] \quad (99)$$

$$= -\frac{8}{\pi\nu_o^4} \left[\int_0^{\nu_o} \tau d\tau \int_0^{\cos^{-1} \left(\frac{\nu}{2\nu_o} \right)} d\phi_\tau (-\tau^2 \cos^2 \phi_\tau + \nu \tau \cos \phi_\tau) \right] \quad (100)$$

$$- \int_0^{\nu/2} d\tau_x \int_0^{\tau_x \frac{2\nu_o}{\nu} \sqrt{1 - \left(\frac{\nu}{2\nu_o} \right)^2}} d\tau_y (-\tau_x^2 + \nu \tau_x) \Pi \left(\frac{\nu}{2\nu_o} \right). \quad (101)$$

For the first inner integral we make use of the following identities

$$\int_0^{\cos^{-1} z} d\phi \cos^2 \phi = \frac{1}{2} z \sqrt{1 - z^2} + \frac{1}{2} \cos^{-1} z, \quad (102)$$

$$\int_0^{\cos^{-1} z} d\phi \cos \phi = \sqrt{1 - z^2}, \quad (103)$$

which results in

$$= -\frac{8}{\pi v_o^4} \left[\int_0^{v_o} d\tau \frac{-\tau^3}{2} \left(\frac{v}{2v_o} \sqrt{1 - \left(\frac{v}{2v_o} \right)^2} + \cos^{-1} \left(\frac{v}{2v_o} \right) \right) + v\tau^2 \sqrt{1 - \left(\frac{v}{2v_o} \right)^2} \right. \\ \left. \int_0^{v/2} d\tau_x \int_0^{\tau_x \frac{2v_o}{v} \sqrt{1 - \left(\frac{v}{2v_o} \right)^2}} d\tau_y (-\tau_x^2 + v\tau_x) \right] \Pi \left(\frac{v}{2v_o} \right), \quad (104)$$

$$= -\frac{8}{\pi v_o^4} \left[\frac{-v_o^4}{8} \left(\frac{v}{2v_o} \sqrt{1 - \left(\frac{v}{2v_o} \right)^2} + \arccos \left(\frac{v}{2v_o} \right) \right) + \frac{2v_o^4}{3} \frac{v}{2v_o} \sqrt{1 - \left(\frac{v}{2v_o} \right)^2} \right. \\ \left. - \frac{5v^2 v_o^2}{48} \frac{v}{2v_o} \sqrt{1 - \left(\frac{v}{2v_o} \right)^2} \right] \Pi \left(\frac{v}{2v_o} \right), \quad (105)$$

$$= \frac{1}{\pi} \left[\left(\frac{v}{2v_o} \sqrt{1 - \left(\frac{v}{2v_o} \right)^2} + \arccos \left(\frac{v}{2v_o} \right) \right) - \frac{16}{3} \frac{v}{2v_o} \sqrt{1 - \left(\frac{v}{2v_o} \right)^2} \right. \\ \left. + \frac{5v^2}{6v_o^2} \frac{v}{2v_o} \sqrt{1 - \left(\frac{v}{2v_o} \right)^2} \right] \Pi \left(\frac{v}{2v_o} \right), \quad (106)$$

$$= \frac{1}{\pi} \left[\arccos \left(\frac{v}{2v_o} \right) - \left(\frac{13}{3} - \frac{5v^2}{6v_o^2} \right) \frac{v}{2v_o} \sqrt{1 - \left(\frac{v}{2v_o} \right)^2} \right] \Pi \left(\frac{v}{2v_o} \right), \quad (107)$$

$$= \frac{1}{\pi} \left[\arccos \left(\frac{v}{2v_o} \right) - \frac{1}{3} \left[13 - 10 \left(\frac{v}{2v_o} \right)^2 \right] \frac{v}{2v_o} \sqrt{1 - \left(\frac{v}{2v_o} \right)^2} \right] \Pi \left(\frac{v}{2v_o} \right). \quad (108)$$

Next we evaluate the autocorrelation for shifts along the y axis

$$\frac{-2}{\pi v_o^4} \left\{ \left[v_x \Pi \left(\frac{v}{v_o} \right) \right] \star_2^y \left[v_x \Pi \left(\frac{v}{v_o} \right) \right] \right\} = \quad (109)$$

$$= \frac{-8}{\pi v_o^4} \left[\int_0^{v_o} d\tau \tau \int_0^{\cos^{-1} \left(\frac{v}{2v_o} \right)} d\phi_\tau (-\tau^2 \sin^2 \phi_\tau) - \int_0^{v/2} d\tau_x \int_0^{\tau_x \frac{2v_o}{v} \sqrt{1 - \left(\frac{v}{2v_o} \right)^2}} d\tau_y (-\tau_y^2) \right] \Pi \left(\frac{v}{2v_o} \right). \quad (110)$$

For the first inner integral we make use of

$$\int_0^{\cos^{-1} z} d\phi \sin^2 \phi = -\frac{1}{2} z \sqrt{1 - z^2} + \frac{1}{2} \cos^{-1}(z). \quad (111)$$

This results in

$$= \frac{-8}{\pi \nu_o^4} \left[\int_0^{\nu_o} d\tau \frac{-\tau^3}{2} \left(\frac{-\nu}{2\nu_o} \sqrt{1 - \left(\frac{\nu}{2\nu_o} \right)^2} + \cos^{-1} \left(\frac{\nu}{2a} \right) \right) - \int_0^{\nu/2} d\tau_x \frac{-\tau_x^3}{3} \left(\frac{2\nu_o}{\nu} \sqrt{1 - \left(\frac{\nu}{2\nu_o} \right)^2} \right)^3 \right] \Pi \left(\frac{\nu}{2\nu_o} \right), \quad (112)$$

$$= \frac{-8}{\pi \nu_o^4} \left[\frac{-\nu_o^4}{8} \left(\frac{-\nu}{2\nu_o} \sqrt{1 - \left(\frac{\nu}{2\nu_o} \right)^2} + \cos^{-1} \left(\frac{\nu}{2\nu_o} \right) \right) + \frac{\nu_o^4}{12} \frac{\nu}{2\nu_o} \sqrt{1 - \left(\frac{\nu}{2\nu_o} \right)^2} \right] \Pi \left(\frac{\nu}{2\nu_o} \right), \quad (113)$$

$$= \frac{1}{\pi} \left[\cos^{-1} \left(\frac{\nu}{2\nu_o} \right) - \frac{1}{3} \left[5 - 2 \left(\frac{\nu}{2\nu_o} \right)^2 \right] \frac{\nu}{2\nu_o} \sqrt{1 - \left(\frac{\nu}{2\nu_o} \right)^2} \right] \Pi \left(\frac{\nu}{2\nu_o} \right). \quad (114)$$

Taking the sum of Eqs. 108 and 114 gives the final result

$$A_2(\nu) = \frac{2}{\pi} \left\{ \cos^{-1} \left(\frac{\nu}{2\nu_o} \right) - \left[3 - 2 \left(\frac{\nu}{2\nu_o} \right)^2 \right] \frac{\nu}{2\nu_o} \sqrt{1 - \left(\frac{\nu}{2\nu_o} \right)^2} \right\} \Pi \left(\frac{\nu}{2\nu_o} \right). \quad (115)$$